11

Implantation Damage Formation in GaN and ZnO

Katharina Lorenz[1] and Elke Wendler[2]
[1]*Instituto Tecnológico e Nuclear, Instituto Superior Técnico, Universidade Técnica de Lisboa, Sacavém & Centro de Física Nuclear da Universidade de Lisboa, Lisboa*
[2]*Institut für Festkörperphysik, Friedrich-Schiller-Universität Jena, Jena*
[1]*Portugal*
[2]*Germany*

1. Introduction

GaN and ZnO and related group-III-N and group-II-O compounds are wide bandgap semiconductors suitable for the production of optoelectronic as well as high temperature, high frequency and high power electronic devices. While GaN based light emitting diodes and lasers are already realized on an industrial scale, ZnO still suffers from fundamental problems, in particular, the lack of efficient and reproducible p-type doping. Nevertheless, the two materials are considered competitors on the way to novel (opto)electronic applications (Yao & Hong, 2009).

1.1 Basic properties of GaN and ZnO

GaN and ZnO show several common characteristics in structural and optical properties. Besides the wide and direct band gap (3.437 eV in ZnO and 3.510 eV in GaN at low temperature) both materials show a similar valence band structure, and both crystallize preferentially in the wurtzite lattice structure. Fig. 1 illustrates the wurtzite structure that consists of two hexagonal lattices that are shifted relative to each other along the c-axis characterized by the so called u-parameter; one lattice is occupied by the cations (Ga/Zn) and the other by the anions (N/O). Some basic parameters of the two materials are summarized in Table 1. The interest in ZnO is increasing mainly due to its high exciton binding energy allowing efficient short wavelength emitters working at room temperature and due to the availability of inexpensive bulk crystals for homoepitaxial growth.

Another common feature of both semiconductors is their strong resistance to radiation damage (Kucheyev et al., 2004). The latter is an important characteristic for device processing steps involving ion implantation, for example for doping or isolation and for the use of electronic circuits in radiation environments, such as in space or nuclear reactors.

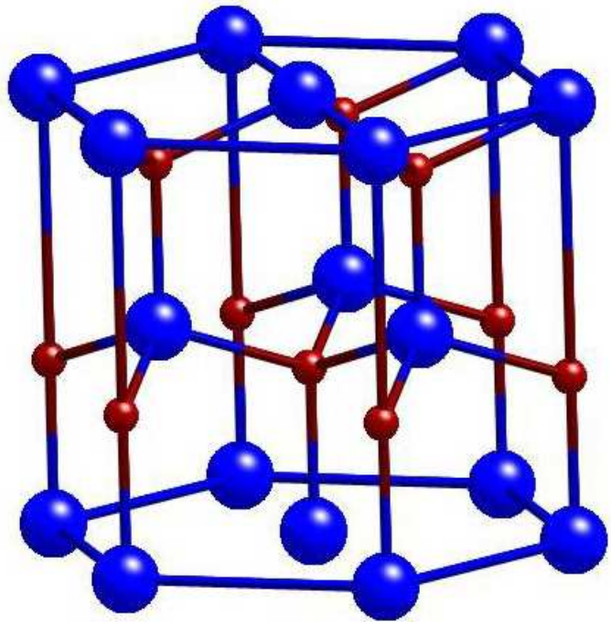

Fig. 1. Schematic of the wurtzite lattice consisting of two simple hexagonal lattices occupied by the cations (Ga/Zn) and the anions (N/O).

	GaN	ZnO
a lattice parameter (Å)[a]	3.189	3.250
c lattice parameter (Å) [a]	5.185	5.204
c/a ratio (ideal 8/3 = 1.633) [a]	1.626	1.601
u-parameter (ideal 3/8 = 0.375) [a]	0.376	0.382
Density (g/cm^3)	6.15[b]	5.675[d]
Band gap (eV) [a]	3.510	3.437
Exciton binding energy (eV) [a]	23.44	60
Melting point (K) [b]	2773	2248
Phillips Ionicity[c]	0.5	0.616

Table 1. Crystal parameters and properties of GaN and ZnO taken from [a](Yao & Hong, 2009), [b](Ioffe Institute, St. Petersburg, http://www.ioffe.rssi.ru/SVA/NSM/), [c](Adachi, 2005), [d](Klingshirn et al., 2010)

1.2 Implantation in GaN and ZnO

While ion implantation is routinely applied in silicon industry for electrical doping or implant isolation, this technique is not very much developed for devices based on wide band gap semiconductors. Nevertheless, prototypes of GaN-based field effect transistors and LEDs employing processing by ion implantation were reported (Pearton et al., 2006) and ion implantation was for example successfully used for optical doping of nitrides using rare earth ions (see e.g. Lorenz et al., 2010a; and references therein). Also magnetic doping for spintronics research was realized for both GaN and ZnO using ion implantation of transition metals or rare earth ions (Pearton et al. 2003, 2004, Brandt et al., 2010). Furthermore many groups investigate the damage formation in ZnO and GaN upon ion

implantation and its effects on the materials' properties (Kucheyev et al., 2001,2004; Ronning et al., 2001; Pearton et al., 2006; and references therein).

The main effect of medium energy ions (several hundred keV range) on materials is caused by energy transfer through atomic collisions (nuclear energy loss). However, other processes active during the implantation are influencing the damage retained after the implantation such as the diffusion of defects (strongly dependent on the implantation temperature) as well as electronic excitations due to the electronic energy loss. The latter can for example change the charge state of defects and influence their diffusivities. Typically, samples are implanted and measured *ex situ* after the implantation to describe the retained lattice damage. An important technique to study implantation damage is Transmission Electron Microscopy (TEM) allowing a direct visualization of defects and the determination of their microscopic nature. Other techniques such as Rutherford backscattering/channelling (RBS/C), X-ray diffraction, Raman scattering, optical spectroscopy or electrical measurements, among others, determine the effect of radiation defects on structural, optical or electrical properties of the materials.

RBS/C allows the determination of defect concentrations with depth resolution and was applied by many groups to investigate implantation damage build-up in GaN and ZnO (e.g. Alves et al., 2003; Jiang et al., 2000; Kucheyev et al., 2001, 2003, 2004; Lorenz et al., 2005, 2009; Wendler et al., 2003). All these reports agree that both GaN and ZnO exhibit strong dynamic annealing during implantation for a vast variety of ion species, energies and implantation temperatures. Dynamic annealing denotes the crystal recovery during the implantation by the recombination of interstitials and vacancies due to close pair recombination as well as defect migration over longer ranges. These effects are of course strongly dependent on the implantation temperature and ionization processes caused by the irradiation. Such processes can be evidenced in RBS/C measurements since they lead to a non-linear increase of defect concentration with ion fluence. Very high amorphisation thresholds are reported for both ZnO and GaN due to this efficient dynamic annealing. In fact, amorphisation of ZnO was only observed for high fluence Si implantation attributed to strong chemical effects (Kucheyev et al., 2003), while heavy ion Au implantation at 77 K (Kucheyev et al., 2003) and Ar implantation at 15 K (Lorenz et al., 2005) did not render ZnO amorphous for fluences as high as 4×10^{16} at./cm^2. GaN can be rendered amorphous at room temperature and below for high fluence implantation (e.g. 2×10^{16} Ar/cm^2 at 300 keV and 15 K. Wendler et al., 2003) but the exact processes are still under debate (Ruterana et al., 2011). Like in ZnO the implanted species have strong effects on the amorphisation behaviour (Kucheyev et al., 2004). In general ZnO was found to be more resistant to radiation damage. One reason for this may be the higher ionicity of the bonds (see Table 1) which was shown to enhance the radiation hardness in semiconductors (see e.g. Trachenko, 2004; Wendler, 2011).

Besides defect recombination, mobility of point defects during the dynamic annealing processes also favours the formation of extended defects such as point defect clusters, stacking faults or dislocation loops. Indeed, TEM investigations for GaN (Wang et al., 2002; Gloux et al., 2006) and ZnO (Perillat-Merceroz et al., 2011) showed the prominence of these defect types in both materials for room temperature implantations.

In this work we review studies on the implantation damage build-up at 15 K in GaN and ZnO measured by RBS/C (Wendler et al., 2003; Lorenz et al., 2005) and discuss similarities

and differences of both materials. At this low temperature thermal diffusion of atoms and defects is minimized. However, defect movement and rearrangement of atoms are still possible, eventually enhanced by lattice strain and electronic excitation processes within ion tracks. Furthermore, the mobility of point defects at temperatures well below room temperature will be demonstrated. Finally, we will discuss the recent advances of optical doping of ZnO and GaN by rare earth implantation.

2. Damage build-up for implantation at 15 K and low temperature annealing

2.1 Experimental details

Ion implantations were performed at 15 K in a special target chamber at the Institut für Festkörperphysik in Jena, where *in situ* RBS/C measurements allow monitoring the defect accumulation without changing the target temperature (Breeger et al., 2001). A schematic of the set-up is shown in Fig. 2. The target chamber is connected to both the 400 keV ion implanter and the 3 MV Tandetron accelerator used to produce the He^+ beam for the RBS/C

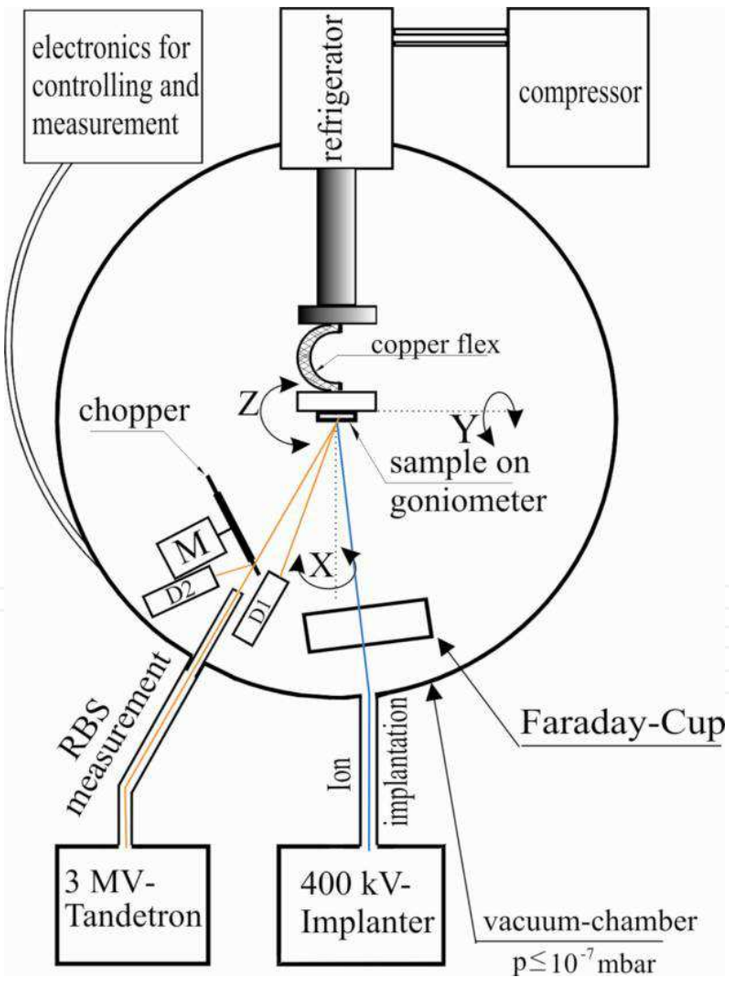

Fig. 2. Schematic representation of the two-beam chamber used for the low temperature *in situ* RBS/C measurements (Breeger et al., 2001).

measurements. In each implantation series a sample is implanted step-wise and after each implantation step a simple rotation of the sample is required to bring it in position for the RBS/C measurement. The sample is mounted on a four axis goniometer and cooled by a closed-cycle He refrigerator. A heating system allows tuning the temperature between 15 K and room temperature. The implantations were carried out with the surface normal tilted by 7° off the ion beam direction to prevent channelling effects. The RBS/C analysis was performed with 1.4 MeV He^+ ions and a Si surface barrier detector at 170°.

Commercial (Eagle-Picher) O-face (0001) ZnO single crystals were implanted with N, Ar, and Er ions to fluences from 1×10^{11} to 7×10^{16} at./cm² using energies of 80, 200, and 380 keV, respectively. GaN layers grown, either by Metal Organic Chemical Vapour Deposition (MOCVD) or by Hydride Vapour Phase Epitaxy (HVPE), on (0001) sapphire substrates were implanted with 300 keV Ar ions to fluences from 3×10^{12} to 4×10^{16} at./cm² as well as with 150 keV O, 780 keV Te, 800 keV Xe or 380 keV Au ions.

2.2 Damage build-up in ZnO

Figure 3 shows RBS/C spectra for Ar implanted ZnO (Wendler et al., 2009). The aligned spectrum of the as-grown sample is also plotted for comparison. The backscattering yields of the aligned spectra increase progressively with the implantation fluence due to the build-up of implantation damage, but even for the highest fluence of 7×10^{16} Ar/cm² the yield remains well below the random backscattering level. As a measure for the produced damage concentration, the difference in minimum yield $\Delta\chi_{min}$ is determined, where $\Delta\chi_{min}$ is given by $\Delta\chi_{min} = (Y_{al} - Y_{al}^{virgin})/Y_{ra}$. Y_{al}^{virgin} and Y_{al} are the RBS yields of the aligned spectra for the unimplanted and implanted sample, respectively, and Y_{ra} is the maximum yield measured in random direction. To calculate the damage level the yields were integrated within windows comprising the entire implanted layer leaving out the surface peak, as indicated in Fig. 3.

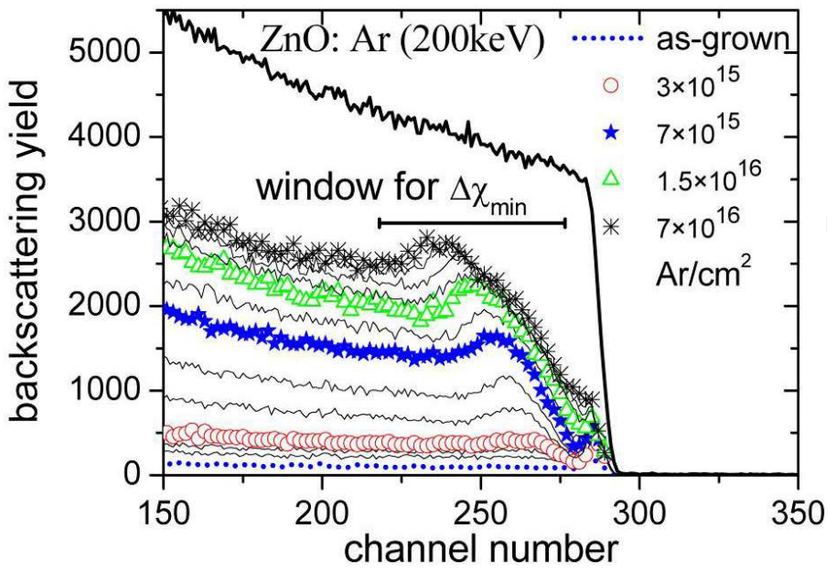

Fig. 3. RBS/C spectra for ZnO implanted with Ar to different fluences compared to the as-grown sample. The window used for the determination of $\Delta\chi_{min}$ is indicated.

Figure 4a shows $\Delta\chi_{min}$ as a function of the ion fluence N_I for the three implanted ion species (Lorenz et al., 2005). The curves do not show a simple linear increase of damage with the fluence but two plateaus can be distinguished, where, within wide fluence ranges, the damage level increases only slightly. Such behaviour is common in materials with strong dynamic annealing effects (Kucheyev et al., 2004).

Four stages of damage production can be distinguished, labelled stage I to IV in Fig. 4, and which are interpreted as follows: In stage I, an almost linear increase of the lattice damage with ion fluence is observed due to the formation of point defects in well separated collision cascades. In stage II the damage saturates; this is attributed to the overlapping of the damage cascades of single ions, allowing for an increased recombination of point defects and the rearrangement of atoms to different defect structures. In stage III the damage increases steeply indicating a slowing down of recombination processes and an enhanced formation of stable defect structures. Stage IV shows a second plateau, being still considerably below the amorphisation level. The last stage was only reached in the case of Ar implantation.

The lines in Fig. 4 are calculated using a simplified version of the Hecking model (Hecking et al., 1986). From the fit of this model to the data, in particular from the first low fluence regime (stage I), the displacement energy for Zn could be estimated to be 65 eV (Lorenz et al., 2005, Wendler, 2011). Although this value is only an upper limit since in-cascade recombination of point defects can occur even at 4 K, the obtained value agrees well with those found by other authors (see Zinkle & Kinoshita, 1997 and references therein).

Simulations with the Monte Carlo program SRIM 2008 (Ziegler et al., 2008) were performed to determine the number of Zn displacements per ion and unit depth at the maximum of the damage profile, N_{displ}, using values for the displacement energies of Zn and O of 65 and 50 eV, respectively. Subsequently, the number of displacements per Zn atom, n_{dpa}, was calculated for each fluence and ion using $n_{dpa}=N_{displ}\cdot N_I/N_0$, where N_I is the ion fluence and $N_0=4.1475\times10^{22}$ Zn/cm^3 the atomic density of Zn in ZnO. This procedure allows the direct comparison of damage build-up curves for different ions or energies. In Fig. 4b the damage build-up curves are re-plotted as a function of n_{dpa}. In this representation the curves for different ions almost overlap. The slight differences observed may be due to the different nature of defects created by ions with largely different masses. The collision cascades are denser in the case of Er implantation, favouring the formation of extended defects and defect clusters, which may be the reason why the steep damage increase in stage III sets in at lower n_{dpa} values than it does for the lighter ions.

Fig. 5 shows selected aligned spectra for N and Er implantation for two different fluences. The fluences were chosen to give approximately the same values of $\Delta\chi_{min}$ for both Er and N implantation and the defect levels DL1 and DL2 corresponding to the selected spectra are marked in Fig. 4 (b). As expected, the fluence to produce a certain damage level is lower for the heavier Er ion. The shape of the aligned spectra is very different for N and Er implantation even for samples showing similar $\Delta\chi_{min}$ values. For N implantation, for both defect levels the expected approximately Gaussian defect distribution is clearly seen from the increased backscattering yield within the implanted region (channel 250 and higher) while the backscattering yield decreases again for deeper layers (below channel 250).

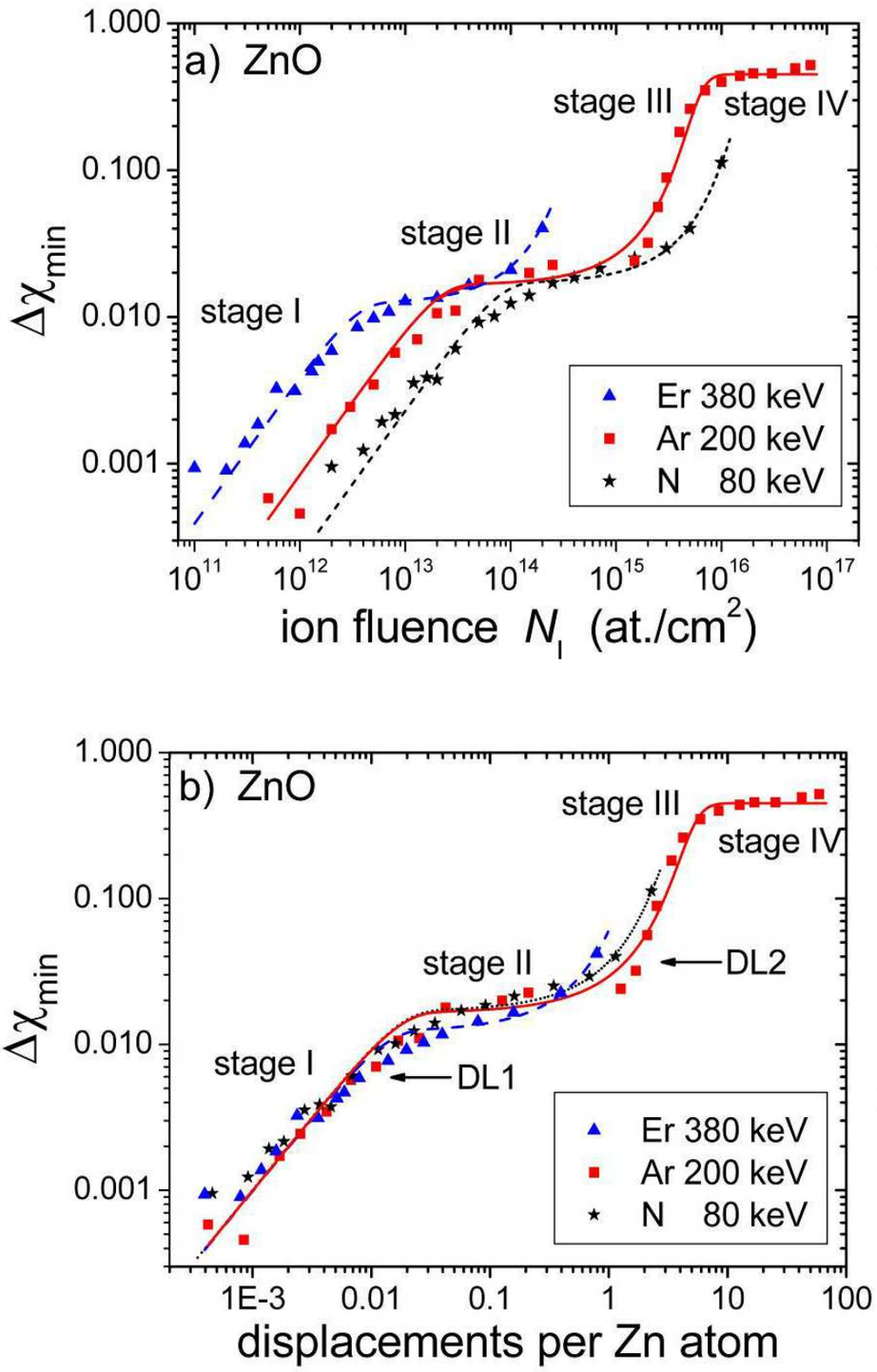

Fig. 4. Difference in minimum yield $\Delta\chi_{min}$ in ZnO as a function of the ion fluence (a) and as a function of the number of displacements per Zn atom, n_{dpa} (b) for 80 keV N, 200 keV Ar and 380 keV Er implantation into ZnO single crystals. The plotted curves are fits based on the defect interaction and amorphisation model of Hecking (Hecking et al., 1986).

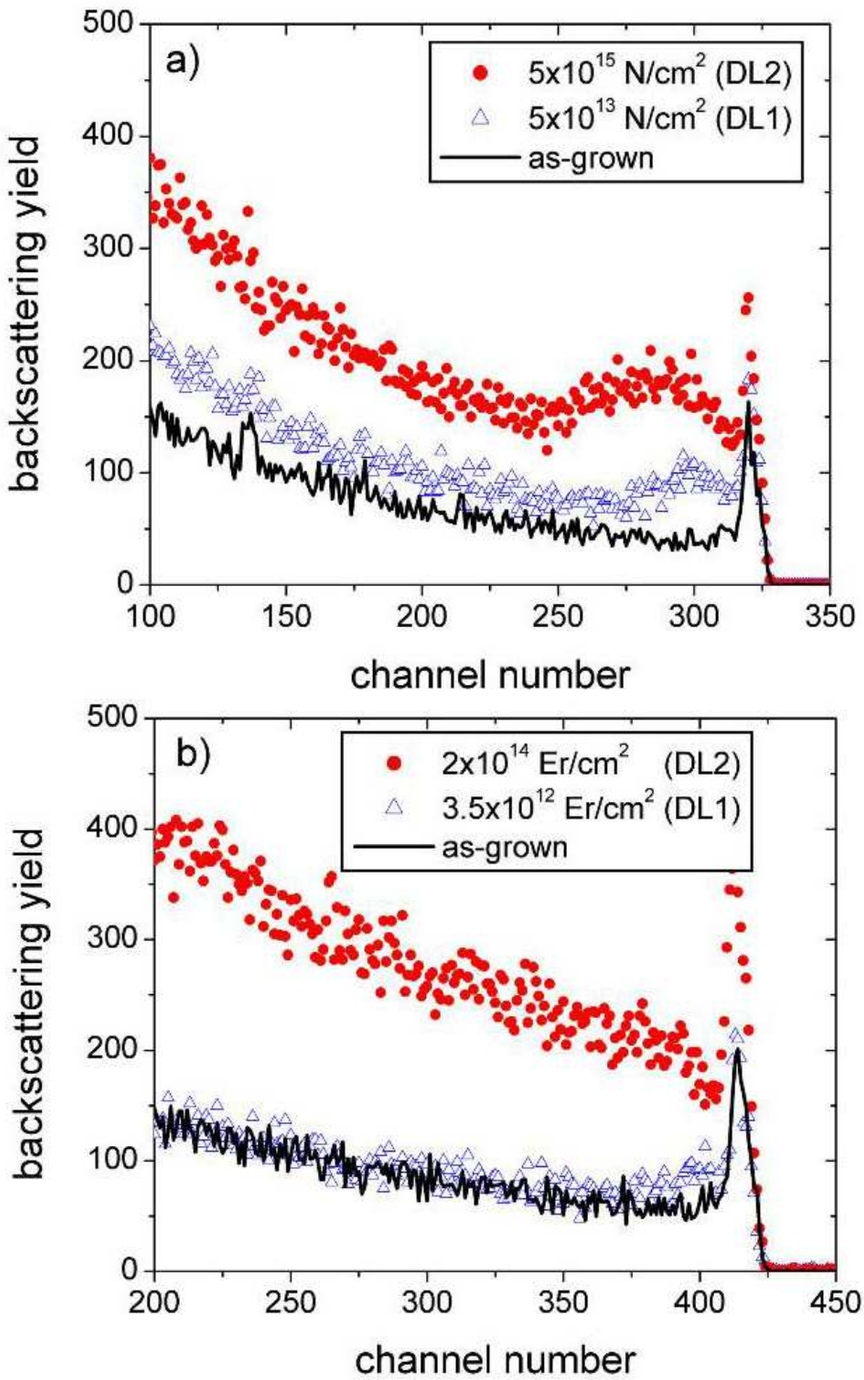

Fig. 5. <0001> aligned RBS/C spectra for ZnO implanted with N (a) and Er (b) to different fluences corresponding to defect levels DL1 and DL2 as marked in Fig. 4b compared to the spectrum of the as-grown sample.

Contrary, for Er implantation to DL2 such a decrease of $\Delta\chi_{min}$ is not observed for depths beyond the implanted region (below channel number 350). It was shown previously that point defects and amorphous zones preferentially lead to direct backscattering at displaced

atoms while stacking faults and dislocation loops rather contribute to the increasing minimum yield by dechannelling of the analyzing beam (see e.g. Feldmann, 1982; Wendler et al., 2009). Therefore, both the high dechannelling rates (Fig. 5b) and the early on-set of stage III in the damage build-up curve (Fig. 4b) for Er suggest that heavy ions facilitate the formation of extended defects like dislocation loops.

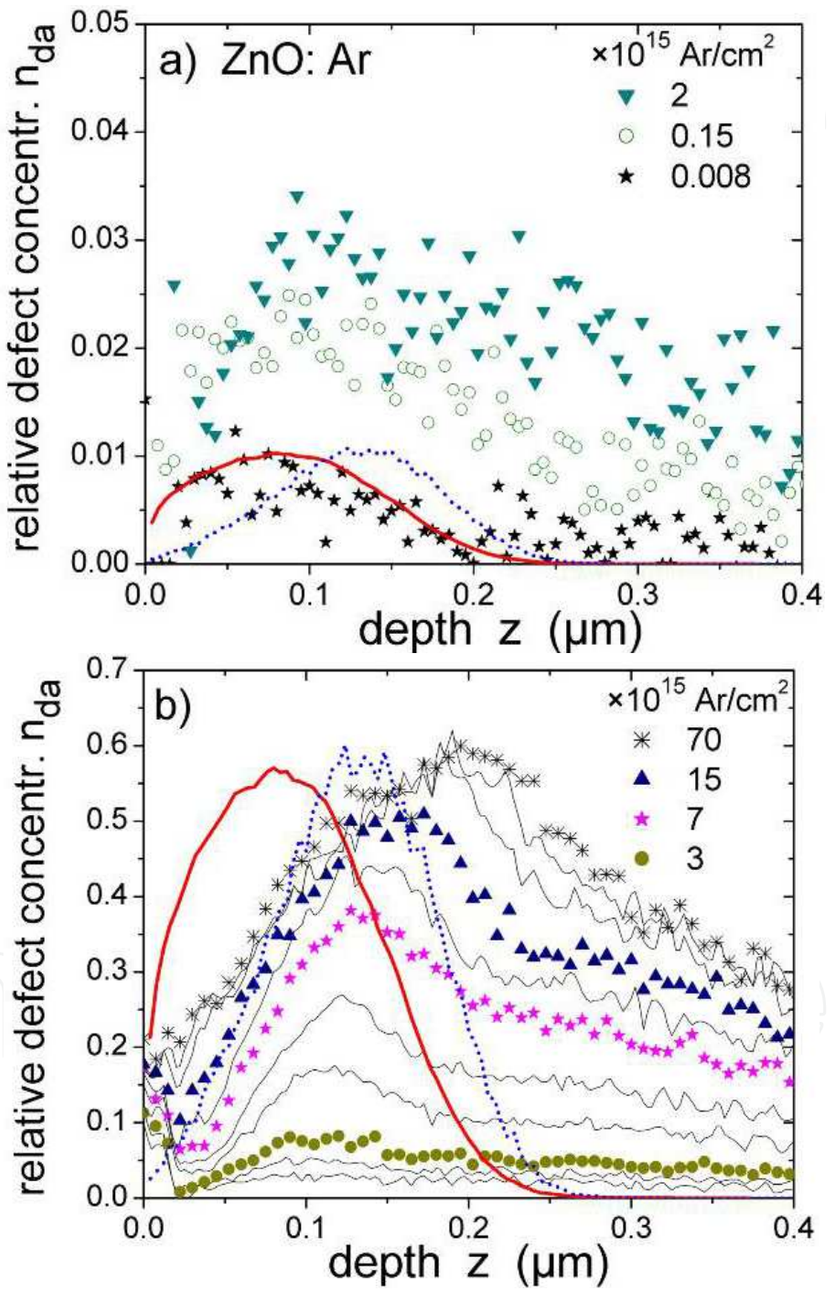

Fig. 6. Defect profiles $n_{da}(z)$ for 200 keV Ar implanted ZnO for various ion fluences. For clarity in (b) only some fluence values are given in the legend. The calculated distributions of primary displacements (red solid line) and implanted ions (blue dashed line) derived from SRIM simulations are given in arbitrary units for comparison.

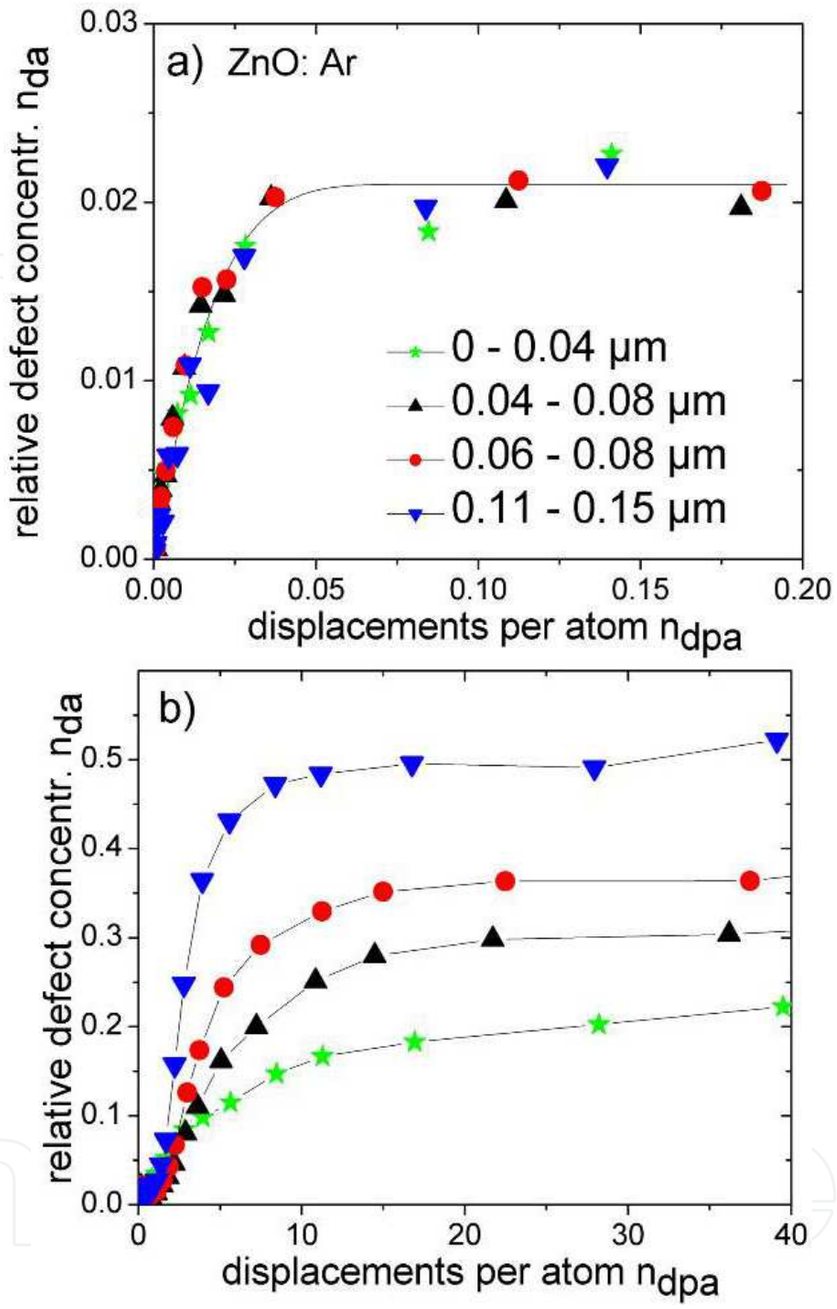

Fig. 7. Relative defect concentration n_{da} at different depth regions versus the corresponding number of displacements per lattice atom n_{dpa} for 200 keV Ar implanted ZnO. Part (a) represents stages I and II and part (b) stages III and IV. The maximum nuclear energy deposition is at 0.06-0.10 µm and the maximum ion concentration at 0.11-0.15 µm (see Fig. 6).

The occurrence of extended defects becomes especially obvious when analyzing the RBS/C spectra in more detail, which is done for Ar implanted ZnO (Wendler et al., 2009). Figure 6 plots the relative concentration of randomly displaced lattice atoms n_{da} versus the depth z (referred to as defect profiles in the following text). The calculated distribution of primary

displacements and the Argon profile, both derived from SRIM simulations, are also included for comparison. The profiles were calculated with the computer code DICADA (Gärtner, 2005) in order to take into account dechannelling. The calculations assume the occurrence of uncorrelated displaced lattice atoms which follow when point defects, clusters of point defects or amorphous zones exist within the implanted layer. These defect types will contribute to the backscattering yield primarily by direct backscattering. Dislocations and stacking faults, on the other hand, will induce strong dechannelling of the analysing beam while the direct backscattering yield is relatively low (Feldman et al., 1982). Behind the implanted layer (below ~0.3 μm), n_{da} should reach zero if the correct type of defects is assumed in the calculation. Within the experimental error this is only the case for very small ion fluences ranging within stage I (see profile for 8×10^{12} Ar/cm² in Fig. 6 (a)). This supports the interpretation that stage I is mainly correlated with the production of point defects. Within stage II strong defect recombination results in a nearly constant defect concentration (see Fig. 4). Furthermore, the profiles in Fig. 6 (a) for 1.5×10^{14} and 2×10^{15} Ar/cm² (both fluences belong to stage II) suggest that there is an extension of the defect distribution towards deeper regions and the defect concentration appears to deviate from zero below the implanted layers. These findings indicate that, within stage II, point defects do not only recombine but extended defects start to form like previously observed for room temperature implantation in ZnO (Perillat-Merceroz et al., 2011). The processes within stages I and II are solely determined by the energy deposition into collision processes. This can be seen from Fig. 4 (b) which compares results for various ion species and shows a perfect overlap of the damage build-up curves and also from Fig. 7 (a) which compares the defect concentration for Ar implanted layers at various depths. The curves overlap for stages I and II.

For stages III and IV, on the other hand, Fig. 4 (b) shows that the curves $\Delta\chi_{min}$ versus n_{dpa} start to split for the various ion species suggesting that the implanted ion species themselves become important for the damage formation. The same result can be deduced from the profiles of the Ar implanted ZnO layers in Fig. 6 (b). The dominant rise of defect concentration within stage III starts at a depth close to that of maximum displacements (see profile for 3×10^{15} in Fig. 6 (b)) but then shifts progressively to larger depths near the implanted Ar ions (see profile for 7×10^{15} Ar/cm² in Fig. 6 (b)). From Fig. 6 (b) it is obvious that for ion fluences within stages III and IV, the calculated profiles do not reach zero and long artificial tails extend far beyond the implanted layer (the maximum range of primary displacements or ions is about 0.3 μm). This suggests that the dechannelling of the analyzing ions within the implanted layer is not correctly treated when assuming only uncorrelated displaced lattice atoms. Therefore the implanted layers must contain extended defects. Most probably the damage consists of a mixture of point defect clusters, stacking faults and dislocation loops. The occurrence of secondary effects in the damage formation, being not solely determined by the nuclear energy deposition for stages III and IV, is also seen in Fig. 7 (b), which shows the defect concentration versus the number of displacements per lattice atom at various depths. In contrast to the results in Fig. 7 (a) no uniform dependence is found.

2.3 Damage build-up in GaN

In Fig. 8 a set of RBS/C spectra is plotted for Ar implanted GaN (Wendler et al., 2003). For low and medium fluences the spectra look similar to those of ZnO and also reveal high dechannelling rates. GaN shows a more pronounced surface damage peak than ZnO. Strong

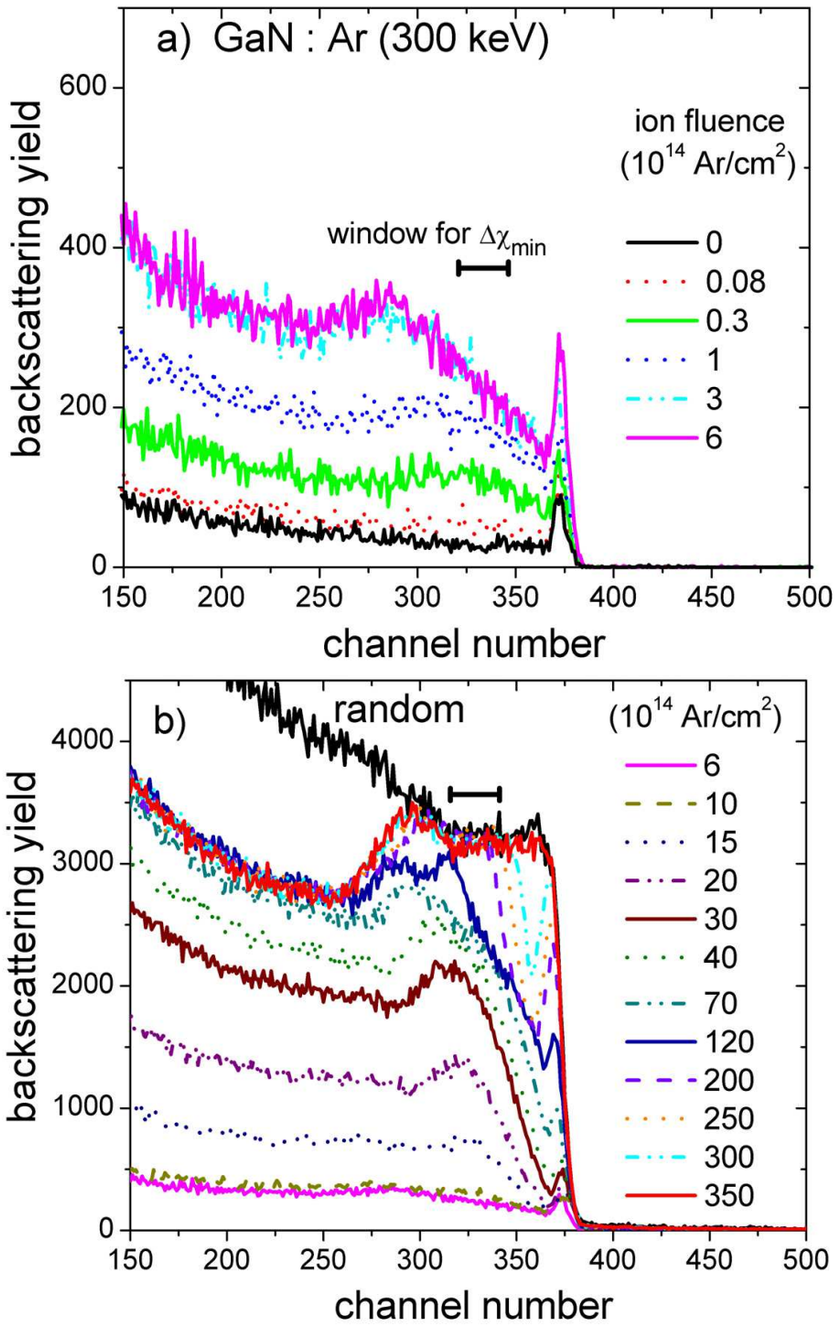

Fig. 8. <0001> aligned RBS/C spectra for GaN implanted with 300 keV Ar to different fluences: a) low ion fluences compared to the as-grown sample and b) high fluences with random spectrum as reference. The window used for the determination of $\Delta\chi_{min}$ is indicated.

surface damage in GaN is also often seen for room temperature implantation usually attributed to the surface acting as a sink for migrating point defects. For fluences between 1.2 and 2×10^{16} Ar/cm^2 the random level is reached (around channel no. 320) which is

commonly taken as an indication for amorphisation. Amorphisation processes in GaN are complex and not well understood. For room temperature implantation it was believed to start at the surface (Kucheyev et al., 2004). However, recent studies indicate that this highly damaged surface layer often consists of randomly oriented nanocrystals rather than an amorphous phase (Ruterana et al., 2011). At 15 K we assume that real amorphisation occurs since dynamic annealing is slowed down, however, from RBS/C measurements alone it is not possible to distinguish amorphous and poly/nanocrystalline material.

To see this effect more clearly in the damage build-up curves, the window for the determination of the $\Delta\chi_{min}$ does not contain the whole implanted layer (see Fig. 8). Fig. 9 (a) shows the damage build-up curves as a function of the fluence for different ion species. In order to compare the results for the various implanted ion species, in Fig. 9 (b) the ion fluence was converted into displacements per Ga atom. Herein a displacement energy of 41eV for Ga and O was taken in the SRIM calculations, with the value for Ga being determined in the same way as for ZnO by fitting the Hecking model to the damage build-up curve (Wendler et al., 2004). This value of the displacement energy is in good agreement with molecular dynamics calculations yielding an average value of 45eV for Ga and 109 eV for N (Nord et al., 2003). The curves in Fig. 9 exhibit five stages of damage formation with the first four being similar as discussed above for ZnO and stage V being the amorphisation which occurs for all ion species (Wendler et al., 2003).

Figure 9 suggests that stage I occurs at given numbers of n_{dpa} independent of the ion species. The first saturation value in stage II is similar for all ion species except for Au ions which may be connected with the fact that in this case the thickness of the implanted layer is only one third of that for the other ion species. Stages III, IV and V shift to larger n_{dpa} values with decreasing mass of the implanted ions, pointing to the role of the implanted ions themselves in these cases. More details about the defect evolution can be seen in the defect profiles plotted in Fig. 10 for Ar implanted GaN, which were calculated as described above for ZnO. Again, simulations for the profiles of primary displacements and Ar are included for comparison. Within stage II there is not only a recombination of defects causing the very weak increase of the defect concentration with rising ion fluence as seen in Fig. 9, but the defect profiles extend into larger depth (see Fig. 10 (a) and (b); stage II for Ar ranges from 1×10^{14} Ar/cm^2 to about 1×10^{15} Ar/cm^2). This indicates the occurrence of some defect mobility even at 15 K and suggests that the formation of more complex defect structures starts already within stage II. The formation of dislocation loops and stacking faults is typically observed in GaN implanted at room temperature (e.g. Kucheyev et al., 2001; Gloux et al., 2006). Their formation may be driven by the large strains induced into the implanted layers by defects and implanted ions which cause an expansion of the *c* lattice parameter as frequently observed by X-ray diffraction (Liu et al., 1997). At the onset of stage III, defect accumulation occurs preferentially at the depth of maximum nuclear energy deposition and within stage IV the defects again extend into larger depth (see Fig. 10 b) and c)). For all ion species studied, amorphous seeds nucleate within a rather narrow layer at a depth below the surface but which is neither that of maximum nuclear energy deposition nor that of maximum ion concentration (see Fig. 10 d)). A further increase of the ion fluence renders the implanted layer amorphous similar to a process known for silicon called ion beam induced interfacial amorphisation (IBIIA) (Priolo & Rimini, 1990). As explained above,

within stage III and IV a complex defect structure of point defect clusters and extended defects is to be expected with the extended defects causing the artificial tails in the defect profiles at depths beyond 0.35 µm. The transformation into the amorphous state is also suggested by the successive disappearance of these tails in the defect profiles with increasing ion fluence (see Fig. 10 d)).

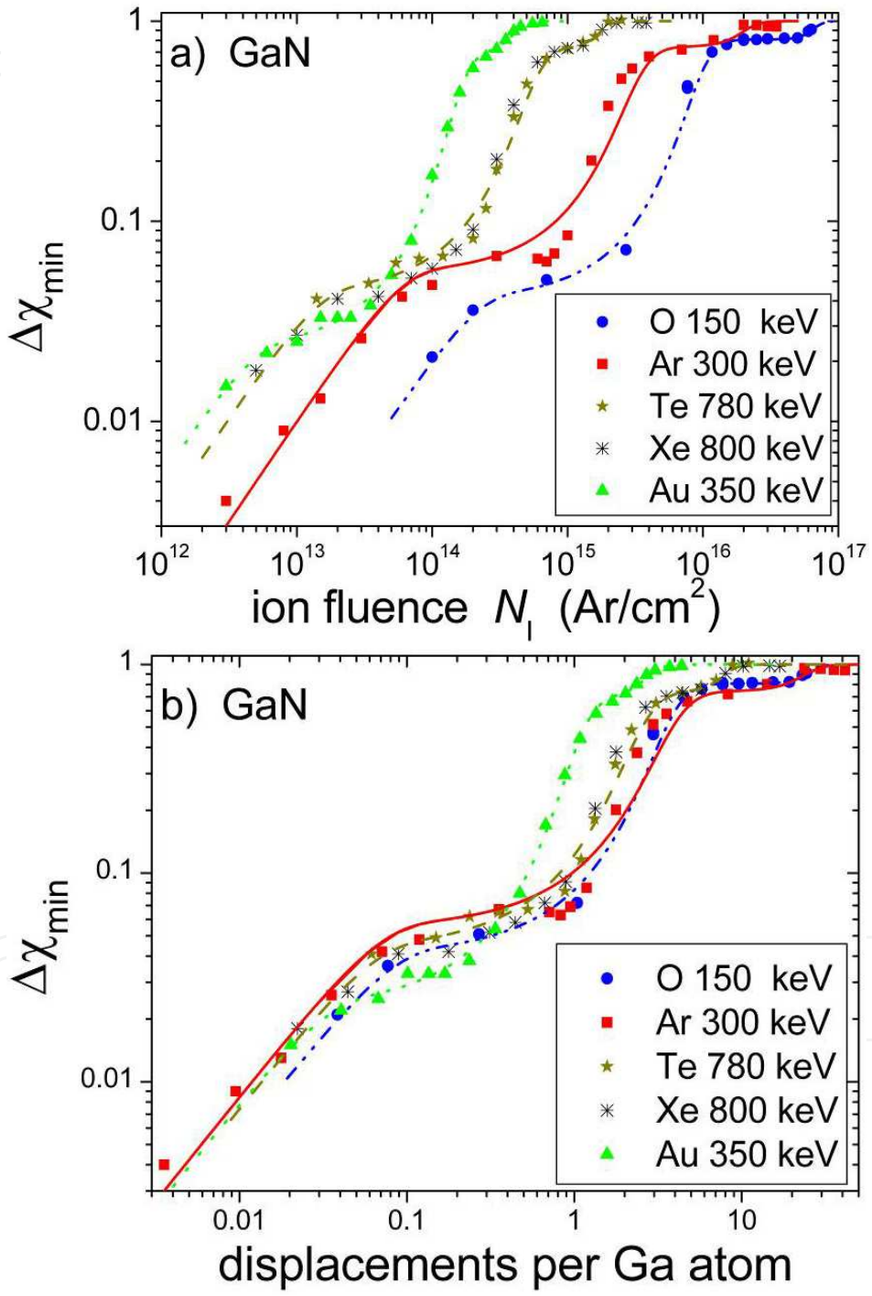

Fig. 9. Difference in minimum yield $\Delta\chi_{min}$ as a function of the fluence (a) and of the number of displacements per Ga atom, n_{dpa} (b) for 150 keV O, 300 keV Ar, 780 keV Te, 800 keV Xe and 350 keV Au implantation into GaN.

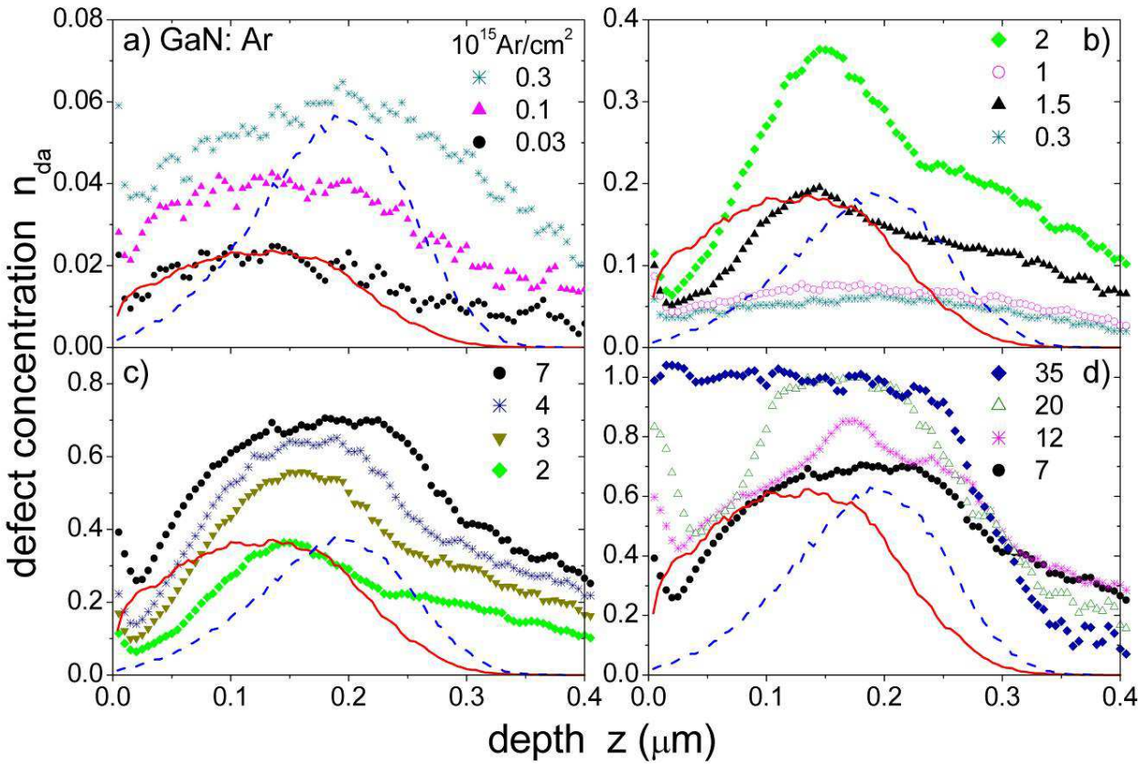

Fig. 10. Defect profiles $n_{da}(z)$ for 300 keV Ar implanted GaN for various ion fluences (in 10^{15} Ar/cm^2). The calculated distributions of primary displacements (solid lines) and implanted ions (dashed lines) are given in arbitrary units for comparison. Notice the different scales of the ordinate.

2.4 Comparison of damage build-up in ZnO and GaN

Both ZnO and GaN were shown above to exhibit strong resistance to implantation damage even at 15 K. Fig. 11 compares directly the damage build-up curves for 15 K Ar implantation in ZnO and GaN. As already mentioned, GaN exhibits a very similar damage accumulation behaviour to ZnO for the first four stages. In contrast to ZnO, in GaN the damage level reaches the random level for the highest fluences (stage V), showing that the channelling effect is completely inhibited and indicating the amorphisation of the material for fluences around 2×10^{16} Ar/cm^2 (n_{dpa}~24) and higher. In ZnO, on the other hand, the damage level stays well below the random level up to the highest fluence of 7×10^{16} Ar/cm^2 (n_{dpa}~59).

For low fluences in stage I (up to n_{dpa}~0.02) very similar damage levels are observed for GaN and ZnO. This is obviously connected with the fact that the masses and displacement energies of the two materials are comparable. In this stage the defect profiles agree well with the distribution of primary displacements calculated with the SRIM code. This suggests that the nuclear energy loss is the primary factor influencing the damage accumulation.

The second stage is interpreted as the fluence regime in which individual collision cascades start to overlap allowing recombination of point defects and the formation of new defect structures. The damage profiles expand towards deeper regions of the sample for both

materials, suggesting that other factors besides the nuclear energy deposition start to influence the damage build-up. The broadened defect distributions and the high dechannelling yields point to a migration of point defects and a formation of extended defects. Since the experiments were carried out at 15 K the defect mobility is most likely induced by athermal processes. High lattice strain upon irradiation has been observed for both materials (Liu et al. 1997; Perillat-Merceroz et al., 2011) and may be one origin for the enhanced defect mobility. Electronic excitations possibly also influence the damage formation. Despite these similarities between the behaviour of GaN and ZnO, in this stage the damage level within the plateau is considerably higher for GaN (n_{da}~0.05) than for ZnO (n_{da}~0.02). This indicates a lower diffusivity of point defects and therefore lower recombination rates or less efficient rearrangement of interstitials to extended defects in GaN than in ZnO.

In stage III, both materials show a strong increase of implantation damage which occurs at higher n_{dpa} values for ZnO than for GaN. The damage profiles exhibit both a pronounced peak typical for direct backscattering from point defect clusters arising in the implanted zone and strong artificial backscattering tails for the deeper, unimplanted regions of the sample suggesting the formation of stacking faults and dislocation loops. Indeed, for the case of room temperature implantation into GaN the strongly increasing damage level was attributed to both displaced atoms in point defect clusters as well as extended defects (Pagowska et al., 2011). However, in GaN the direct backscattering peak arises at the depth of maximum nuclear energy deposition while for ZnO the maximum of the defect peak also starts in this region but then shifts deeper towards the end of range of the implanted Ar ions. In stage IV the maximum defect level remains almost constant, being

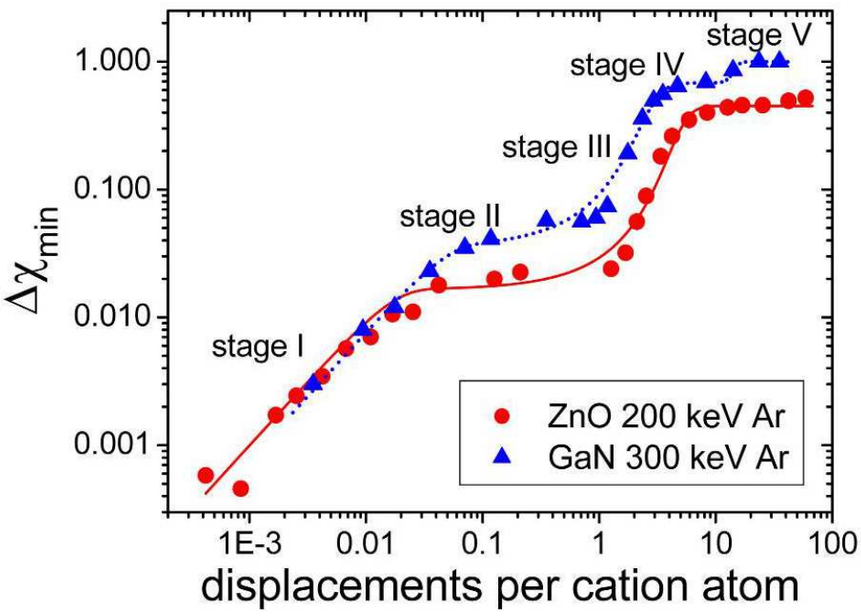

Fig. 11. Difference in minimum yield $\Delta\chi_{min}$ as a function of the number of displacements per cation atom (Ga for GaN and Zn for ZnO) for 200 keV Ar implantation into ZnO and 300 keV Ar implantation into GaN. The plotted curves are fits based on the defect interaction and amorphisation model of Hecking (Hecking et al., 1986).

lower in ZnO than in GaN, showing again its better radiation resistance. In GaN we observe a widening of the defect profile towards the surface and the bulk. For ZnO the shape of the defect profile remains similar to that for stage III and the defect distribution only widens slightly towards deeper regions. The different shapes of the defect profiles for GaN and ZnO in stages III and IV indicate a different microscopic structure within the implanted layers in the two materials.

Finally amorphisation is only reached for GaN (stage V). Amorphous seeds nucleate at a depth with both high damage and high impurity concentration and grow during further irradiation. Contrary, ZnO could not be rendered amorphous even for the highest fluence of 7×10^{16} Ar/cm^2.

2.5 Low temperature annealing of implantation damage

In order to investigate the mobility of defects (in particular Zn and Ga interstitials), annealing experiments were performed at temperatures between 15 K and 250 K (Lorenz et al., 2005, 2011). Samples were first implanted at 15 K to a certain fluence. Then isochronal annealing steps were performed up to 250 K by heating the sample up to a certain temperature for 10 min and then cooling it back to 15 K in order to perform the RBS/C measurement.

Fig. 12 shows $\Delta\chi_{min}$ values as a function of the annealing temperature after 15 K implantation of 2×10^{12} Er/cm^2 into ZnO and 1.5×10^{13} Ar/cm^2 into GaN, corresponding to stage I for which mainly point defects are to be expected. Both materials show partial recovery of the lattice at low temperatures. In the case of ZnO the defect removal starts between 80 and 130 K and for GaN the first annealing step at 100 K already reveals a

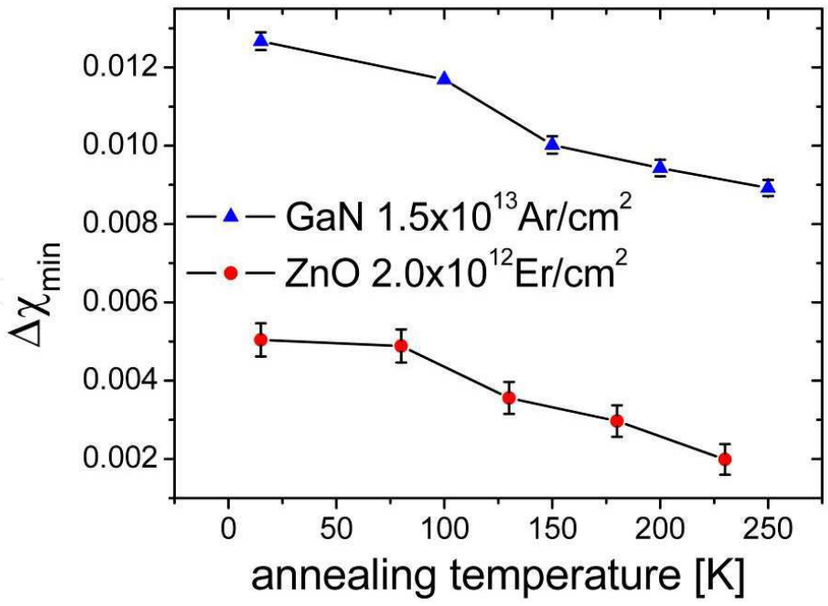

Fig. 12. Difference in minimum yield $\Delta\chi_{min}$ as a function of the annealing temperature after 15 K implantation of 2×10^{12} Er/cm^2 into ZnO and 1.5×10^{13} Ar/cm^2 into GaN. $\Delta\chi_{min}$ was derived using the same window for GaN as shown in Fig. 8 and a window comprising the entire implanted region for ZnO.

decrease of $\Delta\chi_{min}$. The total lattice recovery in the measured temperature range was seen to be better in ZnO. The damage level in ZnO decreases by 60% while that in GaN only decreases by 30%. However, the initial damage level in GaN was higher which may also influence the subsequent annealing results.

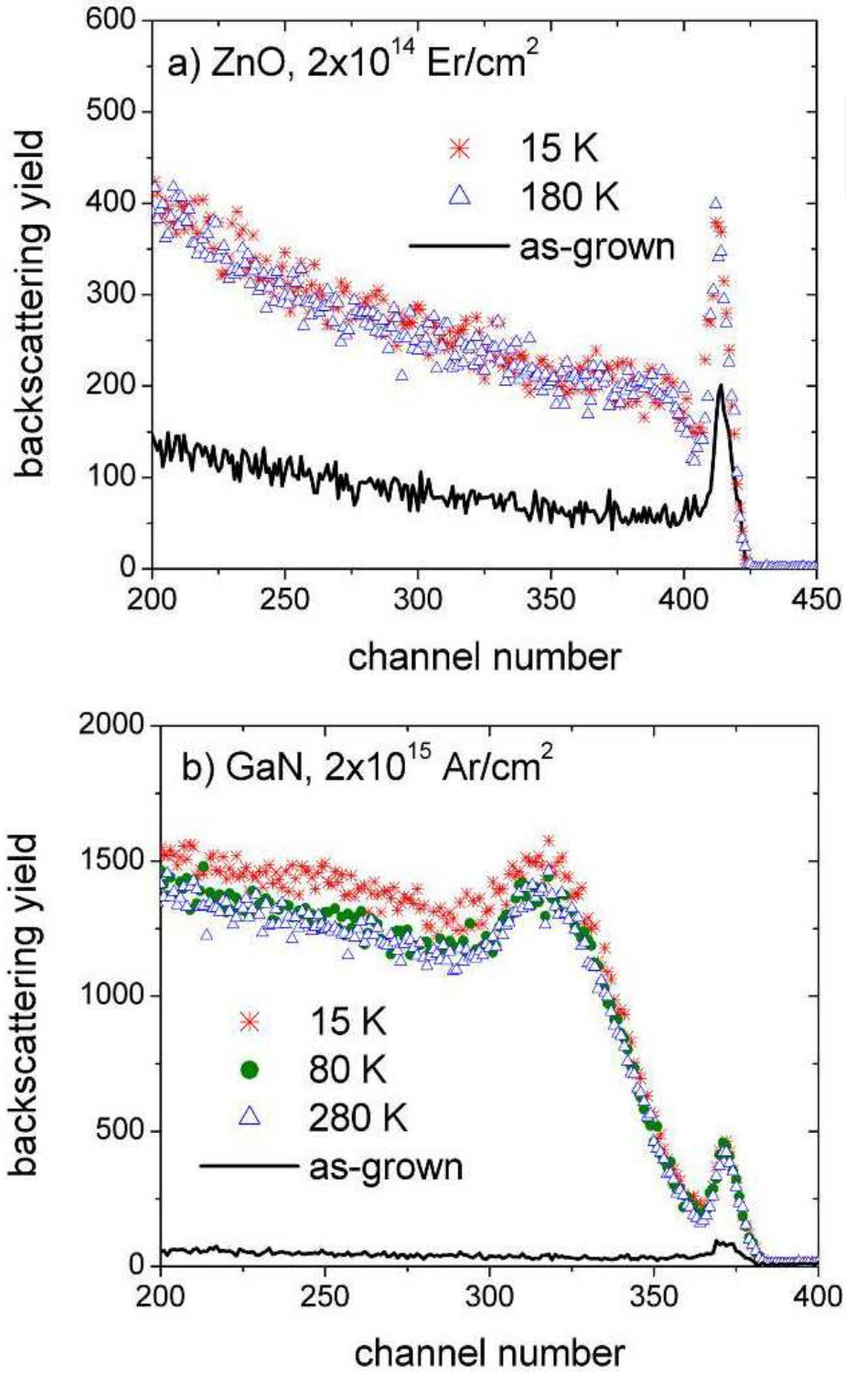

Fig. 13. RBS/C aligned spectra for different annealing temperatures after 15 K implantation of 2×10^{14} Er/cm^2 into ZnO (a) and 2×10^{15} Ar/cm^2 into GaN (b).

To investigate the low temperature defect annealing for higher damage levels ZnO was implanted to a fluence of 2×10^{14} Er/cm^2 and GaN to a fluence of 2×10^{15} Ar/cm^2, both fluences corresponding to stage III (see Figs. 4 and 9). RBS/C aligned spectra after the implantation and different annealing steps are shown in Fig. 13. In the case of ZnO no defect removal is observed up to 180 K, the highest temperature applied. In the case of GaN a very slight recovery of the crystal occurs after annealing at 80 K but increasing the temperature further has no effect on the spectra. The annealing in GaN occurs mainly in a deep region beyond the main defect peak.

We see a clear lattice recovery for fluences corresponding to stage I where mainly point defects are expected. This finding indicates that point defects in both materials are mobile at temperatures as low as 100 K. In ZnO annealing of point defects created by electron irradiation was seen to occur in several steps starting at 110 K in good agreement with our observations (Gorelkinskii and Watkins, 2004). Also in the case of GaN indications were found for a long range motion of an intrinsic defect starting at about 100 K (Chow et al., 2000).

In contrast to the high mobility of point defects in GaN and ZnO, extended defects are known to be thermally stable. A significant reduction of stacking faults in GaN created during implantation was only observed for temperatures well above 1000 ^{o}C (Wojtowicz et al., 2006). Similar results are found for ZnO where in particular basal loops and linear dislocations appeared to be stable after 900 ^{o}C annealing (Perillat-Merceroz et al., 2011). The fact that almost no lattice recovery takes place below room temperature (see Fig. 13) supports our previous assumption that in stages III and IV a complex network of extended defects forms already during implantation at 15 K. The slight annealing in the case of GaN can be attributed to the annealing of remaining mobile point defects similar to the effects seen for the lower fluence (Fig. 12).

3. Rare earth doping and annealing of GaN and ZnO

3.1 Rare earth doped wide bandgap semiconductors

Rare earth (RE) ions incorporated into transparent compounds often prevail in the trivalent RE^{3+} state and show characteristic light emission properties with wavelengths from infrared to ultraviolet, covering the entire visible spectrum. These emission lines originate from transitions within the *4f* electron shell which is only partially filled while it is surrounded by filled *5s* and *5p* orbitals. This shielding is the reason why RE emissions are relatively insensitive to the surrounding matrix (although it is the crystal field of the host matrix that relaxes the selection rules allowing optical transitions which are forbidden in the free ion). Therefore RE^{3+} emission lines are very narrow, show similar wavelengths in different materials and the wavelength is very stable in a wide temperature range. The most prominent example exploiting RE emissions is probably the Nd:YAG laser.

Since Favennec (Favennec et al., 1989) has shown that RE^{3+} emission quenching with temperature is decreasing with increasing energy gap of the semiconductor host, strong research efforts have been undertaken in RE doping of wide bandgap semiconductors like III-nitrides and II-oxides. The wide bandgap of GaN and ZnO furthermore allows light emission in the visible. In fact, GaN was successfully doped with RE ions both by ion implantation or in situ doping techniques and red (Eu, Pr), green (Er, Tb), and blue (Tm) light emission has been achieved (Steckl et al., 2002). Recently the first current injection LED,

operating at low voltages, based on GaN:Eu was realized for doping during epitaxial growth (Nishikawa et al., 2009). Results on RE doping of GaN by ion implantation have been reviewed in (Lorenz et al., 2010a). Optical activation of RE ions in ZnO was found to be more challenging. In both lattices the large RE ions will be more easily incorporated on the cation site. While RE^{3+} in GaN is isoelectronic to Ga, in the case of ZnO some defects or impurities are necessary for charge compensation. RE emission has been reported from polycrystalline pellets and nanomaterials but doping single crystals was less successful (Jadwisienczak et al., 2002, Alves et al., 2003).

Directly after implantation GaN and ZnO samples are typically optically inactive. Implantation defects act as nonradiative recombination paths for excitons and quench both the native luminescence of the host and the RE emissions. Thermal annealing is necessary to remove defects and optically activate the rare earth ions. An empirical rule states that efficient removal of implantation damage should take place during annealing at two thirds of a material's melting temperature (in Kelvin) i.e. ~1600 °C for GaN and ~1200 °C for ZnO. However, at such high temperatures the more volatile N and O start to diffuse out of the samples and induce dissociation of the material. For example GaN was shown to start to dissociate at temperatures as low as 800 °C (Bartels et al., 1999). Also in ZnO outdiffusion of O occurred at temperatures as low as 500 °C if no oxidizing annealing atmosphere was chosen (Pearton et al., 2004).

In GaN, the effect of thermal annealing on RE emission intensity and spectral shape has been intensively studied. Best results were obtained for annealing well above 1000 °C using special measures to protect the surface such as thin AlN capping layers (Lorenz et al., 2004) or extremely high nitrogen pressures (Roqan et al., 2010). Although Europium luminescence intensity is seen to rise strongly with the annealing temperature, implantation defects are thermally very stable and full recovery of structural defects could only be achieved for low implantation fluences. To reach technologically interesting Eu concentrations of > 0.1 at.% high implantation fluences are necessary and it was shown that in such heavily damaged samples residual damage remains even after annealing at temperatures as high as 1450 °C (Lorenz et al., 2010a). Nevertheless, high quality films were produced with emission properties similar to *in situ* doped films used in GaN:Eu LEDs (Lorenz et al., 2010b).

Implantation damage in ZnO after high fluence RE implantation was shown to be fully recovered for 1000 °C annealing in air (Alves et al., 2003), i.e. remarkable 200 °C below the temperature expected for efficient defect removal. Despite this promising result, optical activation of the RE was not achieved. RBS/C shows that the RE diffuses towards the surface during the annealing where it accumulates leading to a second peak in the RBS spectrum (Alves et al., 2003). Furthermore, during the 30 min annealing at 1050 °C about 50% of Er ions were lost (Alves et al., 2003). These results indicate a very low solubility of RE in ZnO. In fact, optical activation of RE implanted single crystalline ZnO was only shown for annealing temperatures below 300 °C (Jadwisienczak et al., 2002), insufficient to effectively remove implantation damage. In some polycrystalline or nanostructured materials, on the other hand, RE emission was observed probably arising from RE residing in grain boundaries or secondary phases (Monteiro et al., 2006).

This chapter does not aim to give an extensive review on RE doping of GaN and ZnO, which would be beyond the scope of this book. In the following we will discuss some RBS/C results in GaN and ZnO in a comparative manner in order to shed some light on the

processes mentioned above leading to efficient RE emission from GaN while RE doping of ZnO remains challenging.

3.2 Experimental details

GaN and ZnO thin films grown by metal organic vapour phase epitaxy (MOCVD) on sapphire substrates were implanted with 160 or 300 keV Eu ions at room temperature. The fluences (1-2×10^{15} Eu/cm^2) were chosen to introduce technologically relevant concentrations of Eu while keeping the implantation damage low. Annealing of the samples was performed at 1000 °C in N_2 atmosphere either for 2 min in a rapid thermal annealing (RTA) equipment or for 20 min in a conventional tube furnace. RBS/C random and aligned spectra as well as full angular scans in the <0001> axis and one additional axis were acquired using 2 MeV He^+ particles.

3.3 Experimental results

Fig. 14 presents RBS/C spectra for 1.3×10^{15} Eu/cm^2 implantation into ZnO (a) and GaN (b) at room temperature and 300 keV. The aligned spectra of the as-grown samples are also shown for comparison. After implantation the minimum yield within the implanted area increases from 4% to 34% for ZnO while for GaN it increases from 2% to 54%. Therefore, like for low temperature implantation, also at room temperature the damage level for a given implantation fluence is lower in the case of ZnO. The surface damage peak is clearly seen for GaN and is absent for ZnO. After annealing GaN for 20 min and ZnO for 2 min at 1000 °C and in nitrogen atmosphere the minimum yields are comparable (~15%). It was shown that for similar implantation conditions, annealing ZnO for 20 min in air could restore the minimum yield of the as-grown sample (Miranda et al., 2011). However, for such treatment the RE is seen to diffuse out of the sample. Therefore in this study RTA was used in an attempt to suppress diffusion. In fact, the Eu profile after annealing did not change as it was shown in (Miranda et al., 2011) but no optical activation of Eu was reached while the GaN sample shown in Fig. 14 b revealed the typical red Eu emission at ~620 nm (Lorenz et al., 2009).

In order to analyse this behaviour in more detail, full angular scans were performed for Eu and Zn/Ga allowing the determination of the lattice site location of Eu in the ZnO and GaN host matrix. Fig. 15 shows these scans for the <0001> axis as well as for an additional axis. Directly after the implantation the <0001> scans for Eu and both Ga and Zn overlap completely suggesting that Eu is located on substitutional lattice sites in both hosts.

In the case of GaN, the minimum yield for Ga decreases after RTA at 1000 °C due to the lattice recovery while the scan for Eu remains basically unchanged. This shows that annealing does not promote the further incorporation of Eu on substitutional sites. Nevertheless, the substitutional fraction remains high after annealing.

It is worth to note that the Eu scan in the tilted $<10\bar{1}1>$ axis shows a slight narrowing compared to the Ga scan indicating that Eu occupies near-substitutional Ga-sites in GaN with a slight displacement along the c-axis (Monteiro et al., 2001). The high substitutional fraction is a prerequisite for efficient RE emission in GaN, in fact, a correlation between substitutional fraction and Eu luminescence intensity was found for implanted samples (Lorenz et al., 2009).

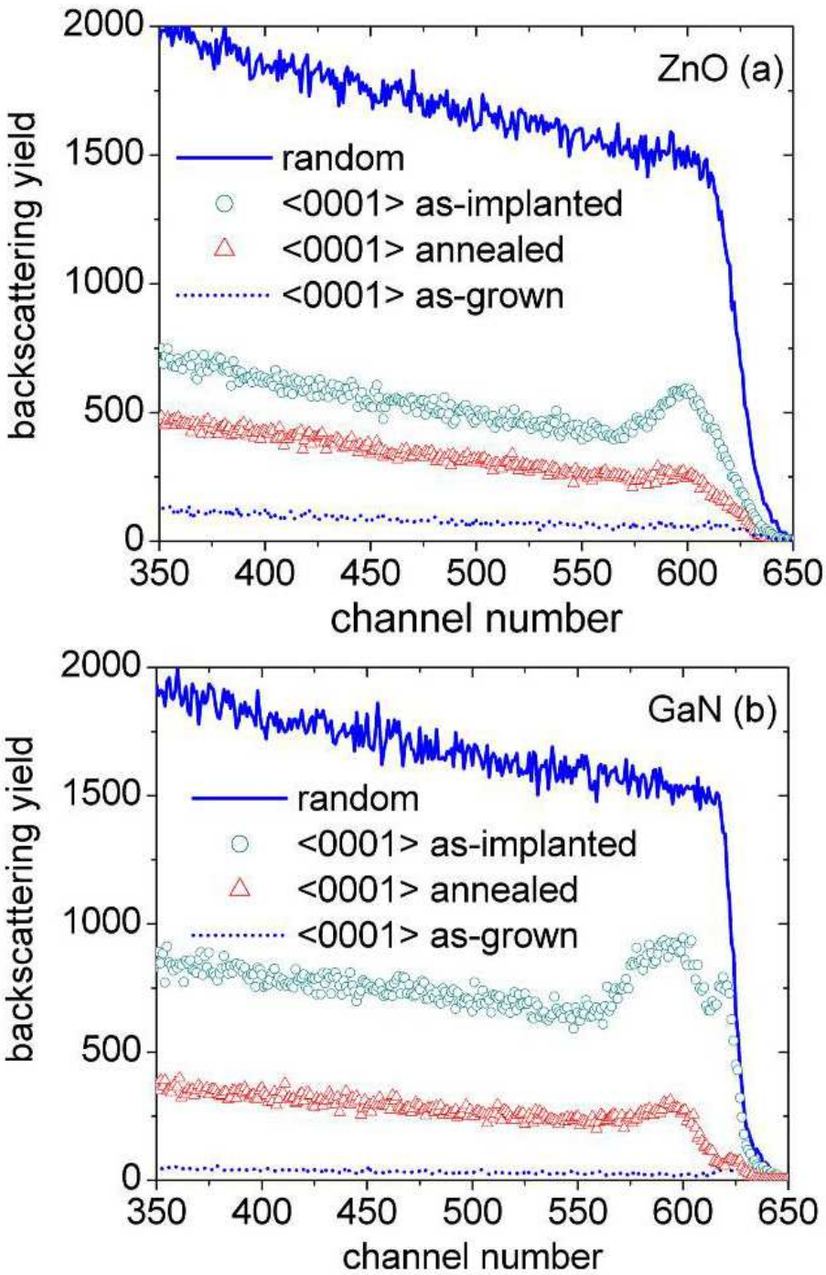

Fig. 14. RBS/C spectra for ZnO (a) and GaN (b) implanted with 1.3×10^{15} Eu/cm^2 with 300 keV at room temperature. The aligned spectra are shown for the as-implanted samples and after annealing at 1000 ^{o}C in N_2 (2 min for ZnO and 20 min for GaN).

For ZnO a different behaviour is observed. RTA successfully removes implantation damage but the minimum yield of Eu is increasing (Fig. 15a). The scans after annealing reveal a very low substitutional fraction of only 13% while the remaining Eu is incorporated on random sites in the ZnO lattice. So although the RTA treatment suppresses long distance diffusion of Eu, it drives the ions out of the substitutional into random lattice sites. A decreasing substitutional fraction with increasing annealing temperature has also been observed using

the emission channelling technique for considerably lower implantation fluences than used in this study (Wahl et al., 2003).

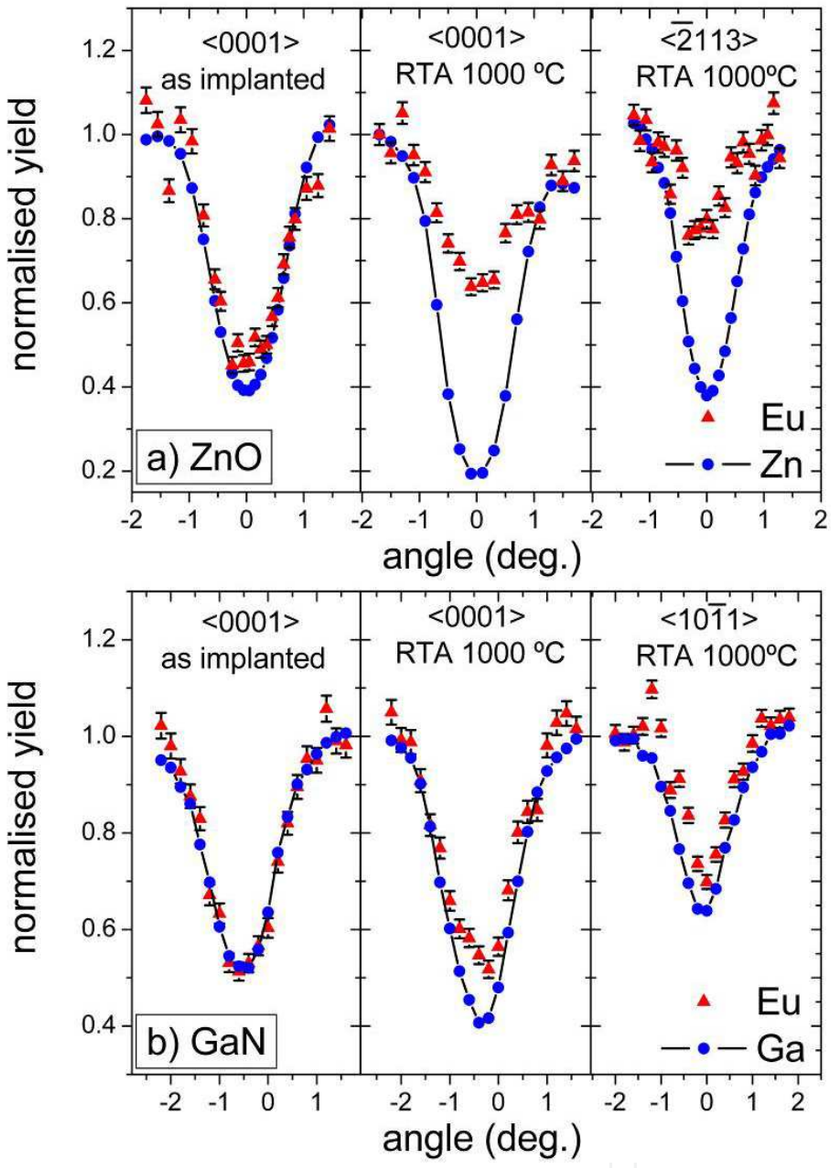

Fig. 15. a) Full angular RBS/C scans in the <0001> and the < $\bar{2}$113 > axes for ZnO implanted to 1.3×10^{15} Eu/cm² with 300 keV at room temperature. b) Full angular RBS/C scans in the <0001> and the < 10$\bar{1}$1 > axes for GaN implanted to 1.5×10^{15} Eu/cm² with 160 keV at room temperature. Both samples were annealed for 2 min in N_2 atmosphere in a rapid thermal annealing (RTA) equipment.

The exact reasons for the difficulty to achieve optical activation of RE ions implanted into ZnO are still under debate. Radiative transitions may be suppressed due to the microstructure in the direct vicinity of the RE ions which may possess an unsuited crystal field or promote non-radiative recombination. Optical activation of implanted RE ions in

ZnO was reported for annealing at 150 °C but the emission gradually vanished with increasing annealing temperature (Jadwisienczak et al., 2002). These results together with the structural results discussed before indicate that the observed change of lattice site of the RE ions during annealing leads to the suppression of RE luminescence.

4. Summary and conclusions

The radiation damage formation upon low temperature ion implantation has been compared for GaN and ZnO. It was shown that both materials exhibit strong dynamic annealing effects even at 15 K. The damage build-up with fluence was found to proceed in a similar way for GaN and ZnO for low and intermediate fluences. Several stages could be distinguished in the damage formation processes. For low ion fluences an almost linear increase of damage with the ion fluence is observed attributed to the formation of point defects in isolated collision cascades (stage I). When the damaged regions produced by single ions start to overlap, vacancies and interstitials can recombine resulting in a plateau-like slow increase of the damage level (stage II). Furthermore our results point to a long range migration and the formation of extended defects within stage II driven by athermal processes. For higher fluences more stable defect complexes form (stage III) and the damage level increases steeply before reaching a second plateau (stage IV). It can be assumed that within stages III and IV a complex network of extended defects (dislocation loops and stacking faults) and point defect clusters forms, similar as observed for room temperature implantation. For high fluences (stage V) GaN amorphises. Contrary, stage V was not reached in ZnO, i.e. it was not rendered amorphous up to the highest fluence applied.

Annealing studies were performed in the temperature range from 15 K to room temperature. For low fluences (stage I) implantation defects are shown to be mobile at temperatures well below room temperature in both semiconductors. However, for higher fluences (stage III) nearly no defect recovery is observed supporting the assumption that thermally stable extended defects have formed even at 15 K.

In conclusion, GaN and ZnO are proved to be radiation resistant even during implantation at very low temperatures. However, the effective defect migration processes favour the formation of extended defects at higher fluences. These defect types are thermally very stable posing a challenge for post-implant annealing which is necessary for implant activation in devices.

Finally, the implantation technique was applied to dope both materials with optically active rare earth (RE) ions. Despite the better radiation properties of ZnO, optical activation of RE could not be achieved which is attributed to the fact that annealing causes a site change of the RE from substitutional to random interstitial sites. For many annealing treatments out-diffusion of the RE is observed due to a low solubility limit. Annealing procedures beyond thermal equilibrium such as laser annealing or taking advantage of the high electronic energy loss by swift heavy ion irradiation may circumvent the problem of site stability of the implanted RE atoms. Further investigations in this direction would be desirable. GaN:RE, on the other hand, shows bright RE emission in the three primary colours. However, the incomplete recovery of implantation damage still poses problems mainly caused by the out-diffusion of N at high temperatures. Above mentioned advanced annealing techniques are worth to be studied as a means to avoid N out-diffusion. Also multi-step

implantation/annealing processes may improve the structural and optical characteristics of implanted GaN. Here fluences should be kept low to avoid the formation of extended defects (preferably corresponding to stage I) and after each implantation step the sample is annealed.

5. Acknowledgements

Funding by FCT Portugal (Ciência 2007, PTDC/CTM/100756/2008) and the German-Portuguese bilateral collaboration program (DAAD-FCT project number 50750957) is gratefully acknowledged.

6. References

Adachi S. (2005). *Properties of Group IV, III/V and II/VI Semiconductors*, Wiley, ISBN 0-470-09032-4, Chichester

Alves E., Rita E., Wahl U., Correia J. G., Monteiro T., Soares J., & Boemare C. (2003). Lattice site location and optical activity of Er implanted ZnO. *Nucl. Instrum. Meth. Phys. Res. B*, Vol. 206, (May 2003), pp. 1047-1051, ISSN 0168-583X

Bartels J., Freitag K., Marques J. G., Soares J. C., & Vianden R. (1999). Incorporation of the transition metal Hf into GaN. *Hyp. Int.,* Vol. 120-121, No. 1-8, (August 1999), pp. 397-402, ISSN 0304-3843

Brandt O., Dhar S., Pérez L., & Sapega V. (2010). High-Temperature Ferromagnetism in the Super-Dilute Magnetic Semiconductor GaN:Gd, In *Rare Earth Doped III-Nitrides for Optoelectronic and Spintronic Applications*, Topics in Applied Physics, Volume 124/2010, O'Donnell K. P. & Dierolf V., pp. 309-342, Springer, ISBN 978-90-481-2876-1, Dordrecht

Breeger B., Wendler E., Trippensee W., Schubert Ch., & Wesch W. (2001). Two-beam irradiation chamber for in situ ion-implantation and RBS at temperatures from 15 K to 300 K. *Nucl. Instrum. Meth. Phys. Res. B*, Vol. 174, No. 1-2, (March 2001), pp. 199-204, ISSN 0168-583X

Chow K. H., Watkins G. D., Usui A. & Mizuta M. (2000). Detection of Interstitial Ga in GaN. *Phys. Rev. Lett.,* Vol. 85, (September 2000), pp. 2761-2764, ISSN 0031-9007

Favennec P.N., L'Haridon H., Salvi M., Moutonnet D., & Le Guillou Y. (1989). Luminescence of Erbium Implanted in Various Semiconductors: IV, III-V and II-VI Materials, *Electronics Lett.*, Vol. 25, No. 11, (May 1989), pp. 718-719, ISSN 0013-5194

Feldman L. C., Mayer J. W., & Picraux S. T. (1982). *Material Analysis by Ion Channeling*, Academic Press, ISBN 0-12-252680-5, New York

Gärtner K. (2005). Modified master equation approach of axial dechannelling in perfect compound crystals. *Nucl. Instrum. Meth. Phys. Res. B*, Vol. 227, No. 4, (October 2004), pp. 522-530, ISSN 0168-583X

Gloux F., Wojtowicz T., Ruterana P., Lorenz K., & Alves E. (2006). Investigation of the crystallographic damage formed in GaN by medium range energy rare earth ion implantation. *J. Appl. Phys.*, Vol. 100, No. 7, (October 2006) p. 073520, ISSN 0021-8979

Gorelkinskii Yu. V. & Watkins G. D. (2004). Defects produced in ZnO by 2.5-MeV electron irradiation at 4.2 K: Study by optical detection of electron paramagnetic resonance. *Phys. Rev. B*, Vol. 69, (March 2004), p. 115212, ISSN 1098-0121

Hecking N., Heidemann K. F., & TeKaat E. (1986). Model of temperature dependent defect interaction and amorphization in crystalline silicon during ion irradiation. *Nucl. Instrum. Meth. Phys. Res. B,* Vol. 15, No. 1-6, (April 1986), pp. 760-764, ISSN 0168-583X

Ioffe Institute, St. Petersburg, http://www.ioffe.rssi.ru/SVA/NSM/ (last accessed August 2011)

Jadwisienczak W. M., Lozykowski H. J., Xu, A., & Patel B. (2002). Visible emission from ZnO doped with rare-earth ions. *Journal of Electronic Materials,* Vol. 31, No. 7, (July 2002), pp. 776-784, ISSN 0361-5235

Jiang W., Weber W. J., & Thevuthasan S. (2000). In situ ion channeling study of gallium disorder and gold profiles in Au-implanted GaN. *J. Appl. Phys.*, Vol. 87, No. 11, (June 2000), pp. 7671-7678, ISSN 0021-8979

Klingshirn C. F., Meyer B. K., Waag A., Hoffmann A., & Geurts J. (2010*). Zinc Oxide from Fundamental Properties towards Novel Applications*, Springer ISBN 978-3-642-10576-0, Heidelberg Dordrecht London New York

Kucheyev S. O., Williams J. S., & Pearton S. J. (2001). Ion implantation into GaN. *Mater. Sci. Eng. R*, Vol. 33, No. 2-3, (May 2001), pp. 51-107, ISSN 0927-796X

Kucheyev S. O., Williams J. S., Jagadish C., Zou J., Evans C., Nelson A. J., & Hamza A. V. (2003). Ion-beam-produced structural defects in ZnO. *Phys. Rev. B*, Vol. 67, (March 2003), p. 094115, ISSN 1098-0121

Kucheyev S. O., Williams J. S., & Jagadish C. (2004). Ion-beam-defect processes in group-III nitrides and ZnO. *Vacuum*, Vol. 73, No. 1, (March 2004), pp. 93–104, ISSN 0042-207X

Liu C., Mensching B., Volz K., Rauschenbach B. (1997). Lattice expansion of Ca and Ar ion implanted GaN. *Appl. Phys. Lett.*, Vol. 71, (October 1997), pp. 2313, ISSN 0003-6951

Lorenz K., Wahl U., Alves E., Dalmasso S., Martin R. W., O'Donnell K. P., Ruffenach S., & Briot O. (2004). High temperature annealing and optical activation of Eu implanted GaN. *Appl. Phys. Lett.,* Vol. 85, No. 14, (October 2004), pp. 2712-2714, ISSN 0003-6951

Lorenz K., Alves E., Wendler E., Bilani O., Wesch W., & Hayes M. (2005). Damage formation and annealing at low temperatures in ion implanted ZnO. *Appl. Phys. Lett.*, Vol. 87, No. 18, (November 2005), p. 191904, ISSN 0003-6951

Lorenz K., Barradas N. P., Alves E., Roqan I. S., Nogales E., Martin R. W., O'Donnell K. P., Gloux F., & Ruterana P. (2009). Structural and optical characterization of Eu-implanted GaN. *J. Phys. D: Appl. Phys.*, Vol. 42, No. 16, (August 2009), pp. 165103, ISSN 0022-3727

Lorenz K., Alves E., Gloux F., & Ruterana P. (2010a). RE Implantation and Annealing of III-Nitrides. In *Rare Earth Doped III-Nitrides for Optoelectronic and Spintronic Applications*, Topics in Applied Physics, Volume 124/2010, O'Donnell K. P. & Dierolf V.,pp. 25-54, Springer, ISBN 978-90-481-2876-1, Dordrecht

Lorenz K., Alves E., Roqan I. S., O'Donnell K. P., Nishikawa A., Fujiwara Y., & Boćkowski M. (2010b). Lattice site location of optical centers in GaN:Eu light emitting diode material grown by organometallic vapor phase epitaxy, *Appl. Phys. Lett.*, Vol 97, No. 11, (September 2010), p. 111911, ISSN 0003-6951

Lorenz K., Peres M., Franco N., Marques J. G., Miranda S. M. C., Magalhães S., Monteiro T., Wesch W., Alves E., & Wendler E. (2011). Radiation damage formation and annealing in GaN and ZnO., *Proceedings of Oxide-based Materials and Devices II, Proc.*

of SPIE Vol. 7940, p. 79400O, ISBN: 978-0-8194-8502-1, San Francisco, USA, January 2011

Miranda S. M. C., Peres M., Monteiro T., Alves E., Sun H. D., Geruschke T., Vianden R., Lorenz K. (2011). Rapid Thermal Annealing of Rare Earth Implanted ZnO Epitaxial Layers. *Optical Materials*, Vol. 33, No. 7, (May 2011), pp. 1139–1142, ISSN 0925-3467

Monteiro T., Boemare C., Soares M. J., Sa-Ferreira R. A., Carlos L. D., Lorenz K., Vianden R., & Alves E. (2001). Photoluminescence and lattice location of Eu and Pr implanted GaN samples, *Physica B*, Vol. 308-310, (December 2001), pp. 22-25, ISSN 0921-4526

Monteiro T., Soares M. J., Neves A., Pereira S., Correia M. R., Peres M., Alves E., Rogers D., Teherani F., Munoz-SanJose V., Trindade T., & Pereira A. (2006). Optical active centres in ZnO samples. *J. Non-Cryst. Solids*, Vol. 352, No. 9-20, (June 2006), pp. 1453–1456, ISSN 0022-3093

Nishikawa A., Kawasaki T., Furukawa N., Terai Y., & Fujiwara Y. (2009). *Appl. Phys. Express*, Vol. 2, No. 7, (July 2009), p. 071004, ISSN 1882-0778

Nord J., Nordlund K., Keinonen J., Albe K. (2003). Molecular dynamics study of defect formation in GaN cascades. *Nucl. Instrum. Meth. Phys. Res. B,* Vol. 202, (November 2003), pp. 93-99, ISSN 0168-583X

Pagowska K., Ratajczak R., Stonert A., Turos A., Nowicki L., Sathish N., Józwika P., & A. Muecklich (2011). RBS/Channeling and TEM Study of Damage Buildup in Ion Bombarded GaN. Acta Physica Polonica A, Vol. 120, No. 1, (July 2011), pp. 153-155, ISSN 0587-4246

Pearton S. J., Abernathy C. R., Overberg M. E., Thaler G. T., Norton D. P., Theodoropoulou N., Hebard A. F., Park Y. D. Ren F., Kim J., & Boatner L. A. (2003). Wide band gap ferromagnetic semiconductors and oxides. *J. Appl. Phys*., Vol. 93, No. 1, (January 2003), pp. 1-13, ISSN 0021-8979

Pearton S. J., Norton D. P., Ip K., Heo Y. W., & Steiner T. (2004). Recent advances in processing of ZnO. *J. Vac. Sci. Technol. B*, Vol. 22, No.3, (May/June 2004) , pp. 932-948, ISSN 0734-211X

Pearton S. J., Abernathy C. R., & Ren F. (2006). *Gallium Nitride Processing for Electronics, Sensors and Spintronics*, Springer, ISBN 1-85233-935-7, London

Perillat-Merceroz G., Gergaud P., Marotel P., Brochen S., Jouneau P.-H., & Feuillet G. (2011). Formation and annealing of dislocation loops induced by nitrogen implantation of ZnO. *J. Appl. Phys.*, Vol. 109, No. 2, (January 2011) p. 023513, ISSN 0021-8979

Priolo F. & Rimini E. (1990). Ion-beam-induced epitaxial crystallization and amorphisation in silicon. *Mat. Sci. Rep.* Vol. 5, No. 6, (June 1990), pp. 319-379, ISSN 0927-796X

Ronning C., Carlson E. P., & Davis R. F. (2001). Ion implantation into gallium nitride, *Physics Reports-Review Section of Physics Letters*, Vol. 351, No. 5, (September 2001), pp. 349-385, ISSN 0370-1573

Roqan I. S., O'Donnell K. P., Martin R. W., Edwards P. R., Song S. F., Vantomme A., Lorenz K., Alves E., & Boćkowski M. (2010). Identification of the prime optical center in GaN:Eu^{3+}. *Phys. Rev. B*, Vol. 81, No. 8, (February 2010), p. 085209, ISSN 1098-0121

Ruterana P., Lacroix B., & Lorenz K. (2011). A mechanism for damage formation in GaN during rare earth ion implantation at medium range energy and room temperature. *J. Appl. Phys.*, Vol. 109, No. 1, (January 2011), p. 013506, ISSN 0021-8979

Steckl A. J., Heikenfeld J. C., Lee D. S., Garter M. J., Baker C. C., Wang Y., & Jones R. (2002). Rare-Earth-Doped GaN: Growth, Properties, and Fabrication of Electroluminescent

Devices. *IEEE J. Sel. Top. Quantum Electron,* Vol. 8, No. 4, (July/August 2002), pp. 749-766, ISSN 1077-260X

Trachenko K. (2004). Understanding resistance to amorphization by radiation damage. *J. Phys.: Condens. Matter*, Vol. 16 (December 2004), pp. R1491–R1515, ISSN 0953-8984

Wahl U., Rita E., Correia J. G., Alves E., & Araujo, J. P. (2003). Implantation site of rare earths in single-crystalline ZnO. *Appl. Phys. Lett.*, Vol. 82, (February 2003), pp. 1173-1175, ISSN 0003-6951

Wang C. M., Jiang W., Weber W. J., & Thomas L. E. (2002). Defect clustering in GaN irradiated with O^+ ions. *J. Mater Res.*, Vol. 17, No. 11, (November 2002), pp. 2945-2952, ISSN 0884-2914

Wendler E., Kamarou A., Alves E., Gärtner K., & Wesch W. (2003). Three-step amorphisation process in ion-implanted GaN at 15 K. *Nucl. Instrum. Meth. Phys. Res. B,* Vol. 206, (May 2003), pp. 1028-1032, ISSN 0168-583X

Wendler E., Wesch W., Alves E., & Kamarou A. (2004). Comparative study of radiation damage in GaN and InGaN by 400 keV Au implantation. *Nucl. Instrum. Meth. Phys. Res. B,* Vol. 218, (June 2004), pp. 36-41, ISSN 0168-583X

Wendler E., Bilani O., Gärtner K., Wesch W., Hayes M., Auret F. D., Lorenz K., & Alves E. (2009). Radiation damage in ZnO ion implanted at 15 K. *Nucl. Instrum. Meth. Phys. Res. B*, Vol. 267, No. 16, (August 2009), pp. 2708–2711, ISSN 0168-583X

Wendler E. (2011). In-Situ RBS Channelling Studies of Ion Implanted Semiconductors and Insulators. *AIP Conf. Proc.,* Vol. 1336, pp. 621-625, *Proceedings of Twenty-First International Conference Application of Accelerators in Research and Industry*, ISBN: 978-0-7354-0891-3, Fort Worth, Texas, USA, August 2010

Wojtowicz T., Gloux F., Ruterana P., Lorenz K., Alves E. (2006). TEM investigation of Tm implanted GaN, the influence of high temperature annealing. *Optical Materials*, Vol. 28, (May 2006), pp. 738-741, ISSN 0925-3467

Yao, T. & Hong S.-K. (Eds.). (2009). *Oxide and Nitride Semiconductors Processing, Properties, and Applications*, Springer, ISBN 978-3-540-88846-8, Berlin Heidelberg.

Ziegler J. F., Biersack J. P., Ziegler M. D. (2008). *SRIM - The Stopping and Range of Ions in Matter,* SRIM Co., ISBN 0-9654207-1-X, Chester, http://www.srim.org/ (last accessed August 2011)

Zinkle S. J. & Kinoshita C. (1997). Defect production in ceramics. *J. Nucl. Mater.*, Vol. 251, (October 1997), pp. 200-217, ISSN 0022-3115

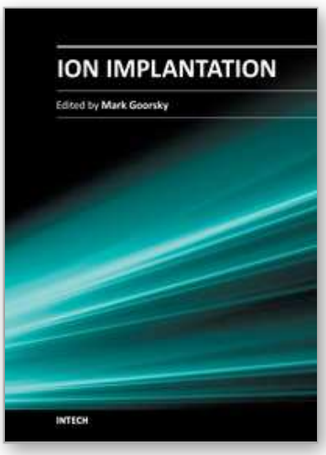

Ion Implantation

Edited by Prof. Mark Goorsky

ISBN 978-953-51-0634-0
Hard cover, 436 pages
Publisher InTech
Published online 30, May, 2012
Published in print edition May, 2012

Ion implantation presents a continuously evolving technology. While the benefits of ion implantation are well recognized for many commercial endeavors, there have been recent developments in this field. Improvements in equipment, understanding of beam-solid interactions, applications to new materials, improved characterization techniques, and more recent developments to use implantation for nanostructure formation point to new directions for ion implantation and are presented in this book.

How to reference

In order to correctly reference this scholarly work, feel free to copy and paste the following:

Katharina Lorenz and Elke Wendler (2012). Implantation Damage Formation in GaN and ZnO, Ion Implantation, Prof. Mark Goorsky (Ed.), ISBN: 978-953-51-0634-0, InTech, Available from: http://www.intechopen.com/books/ion-implantation/implantation-damage-formation-in-gan-and-zno

INTECH
open science | open minds

InTech Europe
University Campus STeP Ri
Slavka Krautzeka 83/A
51000 Rijeka, Croatia
Phone: +385 (51) 770 447
Fax: +385 (51) 686 166
www.intechopen.com

InTech China
Unit 405, Office Block, Hotel Equatorial Shanghai
No.65, Yan An Road (West), Shanghai, 200040, China
中国上海市延安西路65号上海国际贵都大饭店办公楼405单元
Phone: +86-21-62489820
Fax: +86-21-62489821

IntechOpen